J|A|C|S ARTICLES

Published on Web 04/30/2009

The Relationship between Nanoscale Architecture and Charge Transport in Conjugated Nanocrystals Bridged by Multichromophoric Polymers

Reza Dabirian,[†] Vincenzo Palermo,[*,†] Andrea Liscio,[†] Erik Schwartz,[‡] Matthijs B. J. Otten,[‡] Chris E. Finlayson,[§] Emanuele Treossi,[†] Richard H. Friend,[*,§] Gianluca Calestani,[*,⊥] Klaus Müllen,[*,¶] Roeland J. M. Nolte,[‡] Alan E. Rowan,[*,‡] and Paolo Samorì[*,†,■]

Instituto per la Sintesi Organica e la Fotoreattività - Consiglio Nazionale delle Ricerche, Via Gobetti 101, I-40129 Bologna, Italy, Institute for Molecules and Materials - Radboud University, Nijmegen, Toernooiveld 1, 6525 ED Nijmegen, The Netherlands, Cavendish Laboratory - University of Cambridge, J.J. Thomson Avenue, Cambridge CB3 0HE, United Kingdom, Dipartimento di Chimica Generale ed Inorganica, Chimica Analitica, Chimica Fisica - Università degli Studi di Parma, Parco Area delle Scienze 17/A, 43100 Parma, Italy, Max-Planck Institute for Polymer Research, Ackermann 10, 55124 Mainz, Germany, and Nanochemistry Laboratory (ISIS) - Université de Strasbourg and CNRS (UMR 7006) 8 allée Gaspard Monge, F-67000 Strasbourg, France

Received December 13, 2008; E-mail: palermo@isof.cnr.it; a.rowan@science.ru.nl; rhf10@cam.ac.uk; muellen@mpip-mainz.mpg.de; calestg@unipr.it; samori@isis-ulp.org

Abstract: We report on the self-assembly and the electrical characterization of bicomponent films consisting of an organic semiconducting small molecule blended with a rigid polymeric scaffold functionalized in the side chains with monomeric units of the same molecule. The molecule and polymer are a perylene-bis(dicarboximide) monomer (M-PDI) and a perylene-bis(dicarboximide)-functionalized poly(isocyanopeptide) (P-PDI), which have been codeposited on SiO_x and mica substrates from solution. These bicomponent films have been characterized by atomic force microscopy (AFM) and Kelvin probe force microscopy (KPFM), revealing the relationship between architecture and function for various supramolecular nanocrystalline arrangements at a nanometer spatial resolution. Monomer−polymer interactions can be controlled by varying solvent and/or substrate polarity, so that either the monomer packing dictates the polymer morphology or *vice versa*, leading to a morphology exhibiting M-PDI nanocrystals connected with each other by P-PDI polymer wires. Compared to pure M-PDI or P-PDI films, those bicomponent films that possess polymer interconnections between crystallites of the monomer display a significant improvement in electrical connectivity and a 2 orders of magnitude increase in charge carrier mobility within the film, as measured in thin film transistor (TFT) devices. Of a more fundamental interest, our technique allows the bridging of semiconducting crystals, without the formation of injection barriers at the connection points.

1. Introduction

The self-assembly of small molecules to form ordered architectures is currently receiving great interest in particular in connection with the development of electronic devices, where they may find application as new types of electronic materials. Molecular architecture and function are closely related in semiconducting electronic materials.[1−6] It is therefore important to obtain full control over the noncovalent intermolecular interactions ruling molecular aggregation, in order to establish the correlations between molecular and supramolecular structures, with the objective to ultimately be able to modulate the process of hierarchical self-assembly from the subnanometer up to the micrometer scale. Such a control is still not fully possible.[7,8]

While the highest charge mobilities in transistors have been obtained by employing single crystals of small molecules as electroactive architectures,[9,10] typical devices are based on nano- or microcrystalline layers. In such systems the interfaces between different crystals act as bottlenecks for charge transport.[11−13] The generation of highly crystalline films featuring efficient percolation paths for charges is thus a crucial characteristic feature required to achieve an elevated charge transport within an organic thin film.

Monomeric *N*,*N*′-bis(1-ethylpropyl)-3,4:9,10-perylene-bis(dicarboximide) (M-PDI, Scheme 1a) is a well-known organic semiconductor,[14−18] widely used for the fabrication of transis-

[†] Instituto per la Sintesi Organica e la Fotoreattività.
[‡] Institute for Molecules and Materials - Radboud University.
[§] Cavendish Laboratory - University of Cambridge.
[⊥] Dipartimento di Chimica Generale ed Inorganica, Chimica Analitica, Chimica Fisica - Università degli Studi di Parma.
[¶] Max-Planck Institute for Polymer Research.
[■] Nanochemistry Laboratory (ISIS) - Université Louis Pasteur and CNRS (UMR 7006).

(1) Mas-Torrent, M.; Rovira, C. *Chem. Soc. Rev.* **2008**, *37*, 827–838.
(2) Zaumseil, J.; Sirringhaus, H. *Chem. Rev.* **2007**, *107*, 1296–1323.

tors[19−21] and solar cells.[22−25] Recently several groups have shown that this system features interesting self-assembly behavior. Depending on experimental parameters, such as the type of solvent and deposition conditions, different morphologies, including polycrystalline layers composed of needle-like crystals having sizes from tens of nm up to a few μm, were obtained.[19,26−28]

To improve charge transport between the different crystals, an interesting strategy is to use flexible polymeric linkers, which can act as charge-carrying bridges between neighboring nanocrystals. This approach is similar to what occurs spontaneously in polythiophene semicrystalline layers, where a single polymeric chain can span many different neighboring nanocrystalline fibers or domains, thereby bridging them.[29] In order to act as a linker for M-PDI crystals, any chosen polymer should (i) have a sufficiently high rigidity in order to prevent its folding around or into individual nanocrystals, (ii) be able to efficiently transport charges, (iii) be able to be incorporated into or onto the M-PDI crystallites, and (iv) have an electron affinity similar to that of M-PDI in order to avoid the creation of electron traps within the bicomponent film.

Scheme 1. (a) Molecular Structure of M-PDI, (b) Molecular Structure of P-PDI,[a] (c) Schematic Representation of the Helical Structure of P-PDI, with PDI Groups in Red and Backbone in Blue[b]

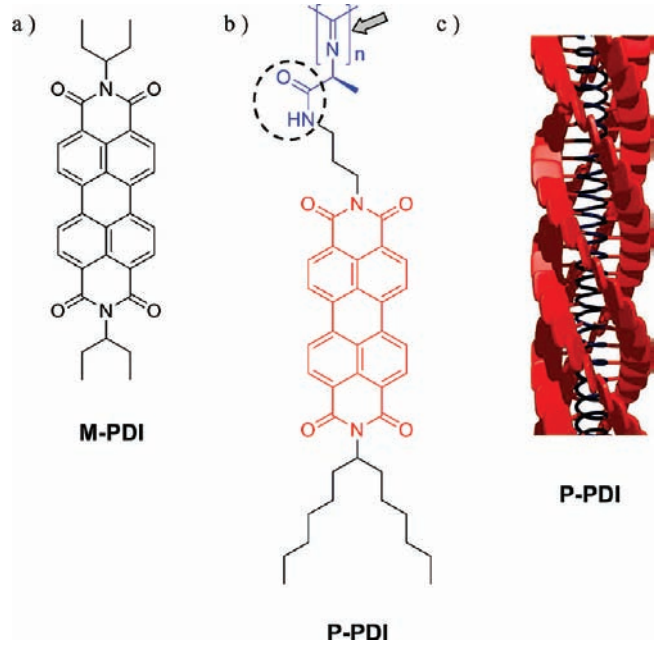

[a] The amide unit, responsible for the stabilization of the helical structure by a hydrogen-bonding network, is encircled. The flexible chain connecting the PDI chromophore to the central backbone is indicated by an arrow. [b] The reciprocal arrangement of PDI groups is just indicative.

With the above criteria in mind we have chosen a very rigid poly(isocyanopeptide) chain equipped with side-chain perylene chromophores (P-PDI)[30−32] as the polymeric building block for improving charge transport between adjacent M-PDI nanocrystals. These P-PDI macromolecules are characterized (Scheme 1b,c) by a rigid helical central backbone[33] providing mechanical rigidity to the architecture, and a lateral functionalization with side chains incorporating PDI units, conveying an electronic function. The main properties of these molecules can be summarized as follows.

(i) Due to the formation of peptide hydrogen bonds between the amide units in the side groups, the polyisocyanide chain adopts a "helter-skelter-like" structure[32] (Scheme 1c) featuring a rather high persistence length of at least 76 nm.[34]

(ii) Recent spectroscopic and computational molecular studies[32,35] showed that the helical structure of P-PDI is fundamental to improve chromophore stacking and thus charge-transport properties of the polymer. The use of a flexible spacer

(3) Coropceanu, V.; Cornil, J.; da Silva, D. A.; Olivier, Y.; Silbey, R.; Brédas, J. L. *Chem. Rev.* **2007**, *107*, 926–952.
(4) Sirringhaus, H. *Adv. Mater.* **2005**, *17*, 2411–2425.
(5) Murphy, A. R.; Fréchet, J. M. J. *Chem. Rev.* **2007**, *107*, 1066–1096.
(6) Jones, B. A.; Facchetti, A.; Wasielewski, M. R.; Marks, T. J. *Adv. Funct. Mater.* **2008**, *18*, 1329–1339.
(7) Palermo, V.; Samorì, P. *Angew. Chem., Int. Ed.* **2007**, *46*, 4428–4432.
(8) van Hameren, R.; Schon, P.; van Buul, A. M.; Hoogboom, J.; Lazarenko, S. V.; Gerritsen, J. W.; Engelkamp, H.; Christianen, P. C. M.; Heus, H. A.; Maan, J. C.; Rasing, T.; Speller, S.; Rowan, A. E.; Elemans, J.; Nolte, R. J. M. *Science* **2006**, *314*, 1433–1436.
(9) Takeya, J.; Yamagishi, M.; Tominari, Y.; Hirahara, R.; Nakazawa, Y.; Nishikawa, T.; Kawase, T.; Shimoda, T.; Ogawa, S. *Appl. Phys. Lett.* **2007**, 90.
(10) Sundar, V. C.; Zaumseil, J.; Podzorov, V.; Menard, E.; Willett, R. L.; Someya, T.; Gershenson, M. E.; Rogers, J. A. *Science* **2004**, *303*, 1644–1646.
(11) Puntambekar, K.; Dong, J. P.; Haugstad, G.; Frisbie, C. D. *Adv. Funct. Mater.* **2006**, *16*, 879–884.
(12) Annibale, P.; Albonetti, C.; Stoliar, P.; Biscarini, F. *J. Phys. Chem. A* **2007**, *111*, 12854–12858.
(13) Zhang, J.; Rabe, J. P.; Koch, N. *Adv. Mater.* **2007**, *20*, 3254–3257.
(14) Wurthner, F. *Chem. Commun.* **2004**, 1564–1579.
(15) Elemans, J.; Van Hameren, R.; Nolte, R. J. M.; Rowan, A. E. *Adv. Mater.* **2006**, *18*, 1251–1266.
(16) Struijk, C. W.; Sieval, A. B.; Dakhorst, J. E. J.; van Dijk, M.; Kimkes, P.; Koehorst, R. B. M.; Donker, H.; Schaafsma, T. J.; Picken, S. J.; van de Craats, A. M.; Warman, J. M.; Zuilhof, H.; Sudholter, E. J. R. *J. Am. Chem. Soc.* **2000**, *122*, 11057–11066.
(17) Nolde, F.; Pisula, W.; Muller, S.; Kohl, C.; Müllen, K. *Chem. Mater.* **2006**, *18*, 3715–3725.
(18) Chesterfield, R. J.; McKeen, J. C.; Newman, C. R.; Ewbank, P. C.; da Silva, D. A.; Brédas, J. L.; Miller, L. L.; Mann, K. R.; Frisbie, C. D. *J. Phys. Chem. B* **2004**, *108*, 19281–19292.
(19) Briseno, A. L.; Mannsfeld, S. C. B.; Reese, C.; Hancock, J. M.; Xiong, Y.; Jenekhe, S. A.; Bao, Z.; Xia, Y. *Nano Lett.* **2007**, *7*, 2847–2853.
(20) Che, Y. K.; Datar, A.; Balakrishnan, K.; Zang, L. *J. Am. Chem. Soc.* **2007**, *129*, 7234–7235.
(21) Tsao, H. N.; Pisula, W.; Liu, Z. H.; Osikowicz, W.; Salaneck, W. R.; Müllen, K. *Adv. Mater.* **2008**, *20*, 2715–2719.
(22) Schmidt-Mende, L.; Fechtenkötter, A.; Müllen, K.; Moons, E.; Friend, R. H.; MacKenzie, J. D. *Science* **2001**, *293*, 1119–1122.
(23) Li, J. L.; Dierschke, F.; Wu, J. S.; Grimsdale, A. C.; Müllen, K. *J. Mater. Chem.* **2006**, *16*, 96–100.
(24) Shin, W. S.; Jeong, H. H.; Kim, M. K.; Jin, S. H.; Kim, M. R.; Lee, J. K.; Lee, J. W.; Gal, Y. S. *J. Mater. Chem.* **2006**, *16*, 384–390.
(25) Dittmer, J. J.; Lazzaroni, R.; Leclère, P.; Moretti, P.; Granstrom, M.; Petritsch, K.; Marseglia, E. A.; Friend, R. H.; Brédas, J. L.; Rost, H.; Holmes, A. B. *Sol. Energy Mater. Sol. Cells* **2000**, *61*, 53–61.
(26) Palermo, V.; Liscio, A.; Gentilini, D.; Nolde, F.; Müllen, K.; Samorì, P. *Small* **2006**, *3*, 161–167.
(27) De Luca, G.; Liscio, A.; Maccagnani, P.; Nolde, F.; Palermo, V.; Müllen, K.; Samorì, P. *Adv. Funct. Mater.* **2007**, *17*, 3791–3798.
(28) Balakrishnan, K.; Datar, A.; Naddo, T.; Huang, J.; Oitker, R.; Yen, M.; Zhao, J.; Zang, L. *J. Am. Chem. Soc.* **2006**, *128*, 7390–7398.
(29) Verilhac, J. M.; LeBlevennec, G.; Djurado, D.; Rieutord, F.; Chouiki, M.; Travers, J. P.; Pron, A. *Synth. Met.* **2006**, *156*, 815–823.
(30) Hernando, J.; de Witte, P. A. J.; van Dijk, E.; Korterik, J.; Nolte, R. J. M.; Rowan, A. E.; Garcia-Parajo, M. F.; van Hulst, N. F. *Angew. Chem., Int. Ed.* **2004**, *43*, 4045–4049.
(31) de Witte, P. A. J.; Hernando, J.; Neuteboom, E. E.; van Dijk, E.; Meskers, S. C. J.; Janssen, R. A. J.; van Hulst, N. F.; Nolte, R. J. M.; Garcia-Parajo, M. F.; Rowan, A. E. *J. Phys. Chem. B* **2006**, *110*, 7803–7812.
(32) Schwartz, E.; et al. *Chem.−Eur. J.* **2009**, *15*, 2536–2547.
(33) Cornelissen, J. J.; Donners, J. J.; de Gelder, R.; Graswinckel, W. S.; Metselaar, G. A.; Rowan, A. E.; Sommerdijk, N. A.; Nolte, R. J. *Science* **2001**, *293*, 676–80.
(34) Samorì, P.; Ecker, C.; Gössl, I.; de Witte, P. A. J.; Cornelissen, J. J. L. M.; Metselaar, G. A.; Otten, M. B. J.; Rowan, A. E.; Nolte, R. J. M.; Rabe, J. P. *Macromolecules* **2002**, *35*, 5290–5294.

between the polymer backbone and the external PDI units allows for optimal spatial arrangement of the latter units (i.e., interacting with each other and eventual stack via $\pi-\pi$ interaction), thereby enabling efficient intramolecular electron transport along the polymer main-chain direction. The electron transfer integrals between adjacent PDIs, calculated by molecular dynamics and intermediate neglect of differential overlap (INDO) methods,[35] gave an average value of 350 cm^{-1}. Compared to single crystals of small molecules such as the oligoacenes,[36] this is a significant value that allows efficient intramolecular electron transport along the polymer.

(iii) These one-dimensional multichromophoric arrays can be considered as a crystalline stack of PDI monomers with a reduced degree of translational freedom; it can therefore be expected that such a macromolecule possesses a strong tendency to interact in solution and on a surface with M-PDI. According to molecular dynamics calculations for the free chain,[35] the most favorable conformation features PDIs oriented along the polymer axis in a "pine tree" motif, with an angle between the PDI long axis and the polymer backbone of 26°. In such a motif the polymer exposes externally one side of the pending PDI aromatic cores, which would therefore easily interact via $\pi-\pi$ stacking with M-PDI eventually present.

(iv) The strong photophysical evidence of "excimer" formation in the P-PDI polymer[30] implies that the HOMO and LUMO levels are very similar to the levels of a stack of PDI monomers; i.e. the intermolecular interactions are of a similar strength.

Thus, this P-PDI fulfills the four conditions indicated above for a linker to act as a charge-carrying bridge.

In this study we describe the formation of M-PDI:P-PDI blend films featuring highly percolated self-assembled architectures, and we report on their structural characterization. The improvement of charge transport in blends with semiconducting polymers has already been demonstrated in the past, using blends of quarter- and polythiophene,[37] polythiophene and dibenzotetrathiafulvalene[38] quarterthiophene and fluorene-based polymers.[39] Although in these previous works a thick layer was used to have good charge mobilities, the transistor "active" layer, i.e. the first nanometer of material at the interface with the gate dielectric, could not be visualized. Hence, in these earlier experiments it could not be excluded, and it was effectively hypothesized by the authors, that most of the charge transport takes place only through one of the components (i.e., the polymer), with the other blend component having only a templating effect on the morphology.

In this contribution instead, we studied specifically the transport in thin, submonolayer networks of M-PDI crystals connected by polymeric P-PDI fibers, mixed on nanometric scales, where a clear identification of the two materials participating in the charge transport is possible by atomic force microscopy. Although using much thicker layers of material would lead to better performance, as already demonstrated in P-PDI-based transistors,[35] in this work priority is given to demonstrate the correlation between nanoscale architecture and charge transport by having an incomplete surface coverage of a few isolated nanostructures whereby the different connectivities with and without the polymer can be clearly visualized by atomic force microscopy.

Our main focus here is on testing blends with minimal amounts of P-PDI because the M-PDI is commercially available in various forms and already mass produced for technological applications.

Atomic force microscopy (AFM)[40−42] has been used to characterize the self-assembled materials on the nanometric and micrometric scale, whereas Kelvin probe force microscopy[43,44] (KPFM) has been employed to measure the surface potential of the M-PDI:P-PDI blends. X-ray diffraction (XRD) has been applied to obtain information on the fine details of the molecular packing and orientation of PDI films prepared by using the different self-assembly procedures and conditions.

Finally, the electrical properties of these bicomponent films have been explored by fabricating prototypes of thin-film transistors (TFT) and by comparing the obtained results with those of transistors incorporating as the electroactive layer the monocomponent M-PDI and P-PDI films.

2. Experimental Procedures

Monomeric *N*,*N*′-bis(1-ethylpropyl)-3,4,9,10-perylenetetracarboxdiimide (M-PDI) was synthesized as previously described.[45] The synthesis and characterization of the polyisocyanide exposing perylene dyes in the periphery (P-PDI) has been described elsewhere.[32] A statistical analysis of the strand lengths revealed a molecular weight of $M_n \approx 1 \times 10^6$ g mol^{-1}. Ultraflat muscovite mica (Ted Pella, Inc.) and Si<100> substrates (Si-Mat, p-type, 0.005 Ωcm) passivated with a thin layer of native SiO_x (∼2 nm) were used as substrates. Before the deposition, mica substrates were cleaved to expose atomically clean and ultraflat layers. Si/SiO_x was polished following a standard RCA procedure. Commercial solvents such as $CHCl_3$, THF, and MeOH (analytical grade) were used without further purification.

2.1. Deposition of Thin M-PDI and/or P-PDI Layers on Si/SiO_x and Mica. Monocomponent samples were prepared by spin-coating 10 μL of M-PDI or P-PDI solutions in either $CHCl_3$, THF, or MeOH onto Si/SiO_x or mica. Typical concentrations used were 500 mg/L and 75 mg/L for M-PDI and P-PDI, respectively. For the preparation of the M-PDI:P-PDI blend films from different solvents, a combined 500 mg/L + 75 mg/L concentrated solution was employed. Solubility in MeOH is poor for M-PDI and very poor for P-PDI. For this reason, in one case the M-PDI:P-PDI blend on Si/SiO_x was prepared through a two-step deposition, consisting of an initial deposition of P-PDI from a solution in THF on Si/SiO_x followed by deposition of a saturated solution of M-PDI in MeOH. The depositions were carried out via spin-coating, with a short solution spreading stage with initial low speed (3 *s* at 500 rpm) followed by a solution drying stage (60 *s* at either 1000 or 2000 rpm).

2.2. Deposition of Bulk Amounts in Glass Capillaries. To investigate the role of the solid surface in the self-assembly of M-PDI in ultrathin layers, macroscopic quantities of M-PDI were

(35) Finlayson, C. E.; Friend, R. H.; Otten, M. B. J.; Schwartz, E.; Cornelissen, J.; Nolte, R. L. M.; Rowan, A. E.; Samorì, P.; Palermo, V.; Liscio, A.; Peneva, K.; Müllen, K.; Trapani, S.; Beljonne, D. *Adv. Funct. Mater.* **2008**, *18*, 3947–3955.
(36) Cheng, Y. C.; Silbey, R. J.; da Silva, D. A.; Calbert, J. P.; Cornil, J.; Brédas, J. L. *J. Chem. Phys.* **2003**, *118*, 3764–3774.
(37) Russell, D. M.; Newsome, C. J.; Li, S. P.; Kugler, T.; Ishida, M.; Shimoda, T. *Appl. Phys. Lett.* **2005**, *87*, 222109.
(38) Kambayashi, T.; Wada, H.; Goto, M.; Mori, T.; Park, B.; Takezoe, H.; Ishikawa, K. *Org. Electron.* **2006**, *7*, 440–444.
(39) Lim, E.; Jung, B. J.; Chikamatsu, M.; Azumi, R.; Yase, K.; Do, L. M.; Shim, H. K. *Org. Electron.* **2008**, *9*, 952–958.
(40) Samorì, P. *Chem. Soc. Rev* **2005**, *34*, 551–561.
(41) Samorì, P.; Surin, M.; Palermo, V.; Lazzaroni, R.; Leclère, P. *Phys. Chem. Chem. Phys.* **2006**, *8*, 3927–3938.
(42) Takano, H.; Kenseth, J. R.; Wong, S.-S.; O'Brien, J. C.; Porter, M. D. *Chem. Rev.* **1999**, *99*, 2845–2890.
(43) Fujihira, M. *Annu. Rev. Mater. Sci.* **1999**, *29*, 353–380.
(44) Palermo, V.; Palma, M.; Samorì, P. *Adv. Mater.* **2006**, *18*, 145–164.
(45) Nolde, F.; Qu, J. Q.; Kohl, C.; Pschirer, N. G.; Reuther, E.; Müllen, K. *Chem.-Eur. J.* **2005**, *11*, 3959–3967.

also crystallized in thin glass capillaries from saturated solutions of different solvents ($CHCl_3$, THF, or MeOH), allowing M-PDI to rearrange in different morphologies according to the solvent used. To favor a thermodynamically driven self-assembly and to increase the concentration of the solution which can be attained at room temperature, the self-assembly from $CHCl_3$ and THF solutions was realized by keeping a constant temperature of 55 °C for 40 h, while in the case of MeOH a 40 h heating at 65 °C was used. XRD measurements were performed both on these bulk samples and on thin layers of M-PDI, prepared as described above.

2.3. Atomic Force Microscopy. Intermittent contact AFM topographical images were recorded by using either a Multimode IIIA microscope (Veeco, Santa Barbara, CA, U.S.A.) equipped with the Extender Electronics module or an Autoprobe CP Research (ThermoMicroscope, Sunnyvale, CA, U.S.A.). The measurements were done under atmospheric conditions at room temperature with line-scan rates of 0.6 − 2.0 Hz. Scan sizes spanning from 20 μm down to 0.5 μm were explored, with a resolution of 512 × 512 pixels using noncontact Si ultralevers (RFESPA5, Veeco) with a spring constant $k < 4$ Nm^{1-}.

2.4. Kelvin Probe Force Microscopy. KPFM measurements were carried out with a Multimode IIIA microscope (Veeco, Santa Barbara, CA, U.S.A.) using a setup already described.[46] In this technique, the electrostatic interaction between a scanning tip and the sample is used to get a quantitative map of the surface potential.[44] In order to obtain a sufficiently large and detectable mechanical deflection, we employed soft ($k < Nm^{1-}$) highly doped Si cantilevers with oscillating frequencies in the range of $60 < \omega < 90$ kHz (SCM-PIT, Veeco). For the sake of simplicity, the substrate was used as reference, and its surface potential (SP) value was set to zero (i.e., $\Delta SP = SP_{perylene} - SP_{substrate}$).

2.5. Characterization by XRD and Optical Microscopy. Single crystal XRD measurements were performed with a Bruker AXS diffractometer equipped with an APEX 2 CCD area detector using Mo Kα radiation. Powder diffraction experiments were performed using Cu Kα radiation either in Debye−Sherrer geometry, with samples in capillary, using a Bruker D8 diffractometer equipped with a double Goebel mirror, or with a Thermo ARL X'tra diffractometer in thin film configuration. XRD patterns were collected with 0.02−0.05° steps and counting times ranging from a few seconds to some tens of seconds per step, depending on sample quantities and experimental conditions.

Optical large-scale analysis of the sample morphology was performed using an optical microscope equipped with a CCD camera.

2.6. Fabrication of Thin Film Transistors. The architecture of the bottom-gate thin-film transistors (TFTs) was developed as follows: silicon substrates, covered by a ~300 nm thick SiO_x gate dielectric layer, were photolithographically patterned with 30 nm thick interdigitated source-drain gold electrodes. The printed devices had channel lengths and widths of 2−20 μm and 1 cm, respectively. The TFT substrates were initially cleaned using standard RCA procedures. To facilitate charge injection at the interfaces, the surfaces of both source-drain electrodes and gate dielectric were modified with self-assembled monolayers.[47−49] To this end, the oxide surface was functionalized by exposing the sample to refluxing hexadimethylsilazane (HMDS) at 150 °C for ~3 h. Subsequently, the source-drain electrodes were functionalized by immersing the sample in a 20 mM dodecanethiol solution in ethanol for approximately 10 min, after which they were rinsed with ethanol and dried with a gentle flow of N_2. The organic semiconductor solutions were deposited on the sample by spin-coating. To counteract the reduced polarity of the silanized SiO_x substrate, the polarity of the solution was varied using $CHCl_3$/THF mixtures. Five arrays of TFT devices were prepared, each using the same total M-PDI and P-PDI concentration of 1800 mg/L, but with varying ratios between the two components. The respective M-PDI:P-PDI ratios were 1:0, 5:1, 1:1, 1:5, 0:1 (in percent, 0%, 17%, 50%, 83%, and 100% P-PDI weight/weight concentration). The solvent was a 1:1 $CHCl_3$/THF (v/v) mixture for all the samples. The depositions were carried out using the same spin-coating parameters as described above, except for a faster (5000 rpm) drying stage.

Scheme 2. Schematic Drawing of Three Hypothetical Outcomes When Codepositing a Monomeric Crystal with Its Corresponding Polymer: (a) No Reciprocal Interference, (b) Self Organization Directed by Nanocrystals, (c) Self Organization Directed by Polymer

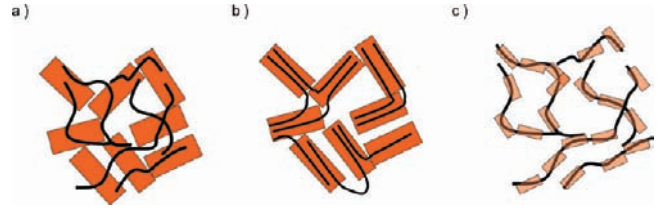

3. Results

3.1. Self-Assembly of Bicomponent M-PDI:P-PDI Films at Surfaces. The hierarchical self-assembly of molecules from solution onto a surface is ruled by the interplay of thermodynamic and kinetic control. While the first is governed by the joint effect of molecule−molecule, molecule−solvent, and molecule−surface interactions, the second is regulated by the solvent evaporation dynamics, the rate of the self-assembly process, and the size and nucleation density of the growing structures.[7] In M-PDI monocomponent films, we found that the morphology can be altered by subtle changes in the molecule−molecule, molecule−solvent and substrate−solvent interactions, leading to the formation of a wide range of different morphologies, spanning from continuous layers, to flat crystals and elongated needles (see Supporting Information and Figure S1). On the other hand, P-PDI chains usually adopt random conformations on surfaces on which they are deposited. Kinetically driven P-PDI deposition on Si/SiO_x (from solutions in $CHCl_3$ or THF) and mica (from solutions in $CHCl_3$) resulted in a random network of thin fibers, generally 2−3 nm thick, indicative of individual polymer chains (Figure S2a,b). In contrast, bundles of fibers were found in the case of depositions from THF on mica with fibers nestling together to form wrapped-up arrangements. The bundles were fractionally thicker (4−8 nm) than the network of fibers observed in the other samples (Figure S2c). The use of MeOH as a solvent for P-PDI was not attempted, since it is known that this polymer is insoluble in this polar medium.

In general three outcomes can be foreseen when codepositing on a surface a monomeric system with its corresponding polymer. In the first case the two components do not interact with each other, with the final morphology being a simple superimposition of the individual deposition patterns (Scheme 2a). In the second case, the monomer tendency to self-assemble in large crystals dominates, and the polymer chain conformations adapt to this morphology being included in one or more than one growing crystals (Scheme 2b). In the third case, the polymer rules, and the final morphology is formed by a kinetically generated network of polymer

(46) Liscio, A.; Palermo, V.; Gentilini, D.; Nolde, F.; Müllen, K.; Samorì, P. *Adv. Funct. Mater.* **2006**, *16*, 1407–1416.
(47) de Boer, B.; Hadipour, A.; Mandoc, M. M.; van Woudenbergh, T.; Blom, P. W. M. *Adv. Mater.* **2005**, *17*, 621–625.
(48) Chua, L. L.; Zaumseil, J.; Chang, J. F.; Ou, E. C. W.; Ho, P. K. H.; Sirringhaus, H.; Friend, R. H. *Nature* **2005**, *434*, 194–199.
(49) Rawcliffe, R.; Shkunov, M.; Heeney, M.; Tierney, S.; McCulloch, I.; Campbell, A. *Chem. Commun.* **2008**, 871–873.

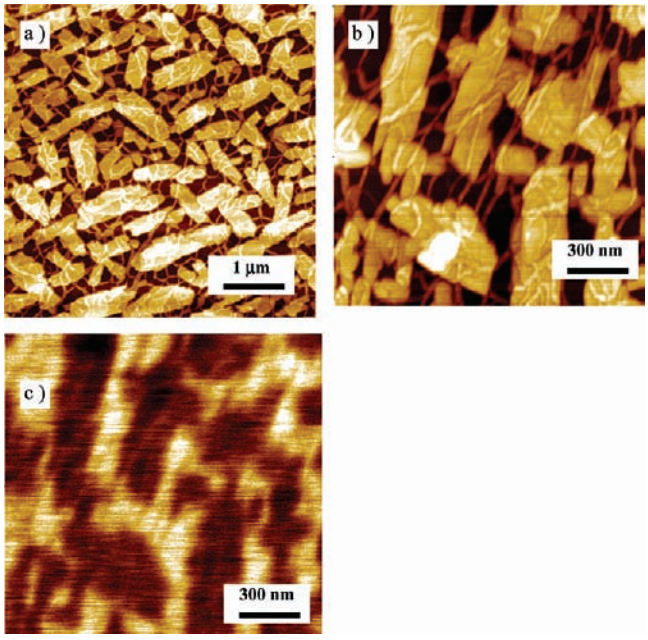

Figure 1. Ultrathin film of blended monomeric M-PDI and P-PDI deposited from $CHCl_3$ on mica: (a,b) AFM height images, (c) KPFM recorded surface potential image of the area shown in (b). *Z*-scales: (a) 14 nm, (b) 15 nm, (c) 125 mV.

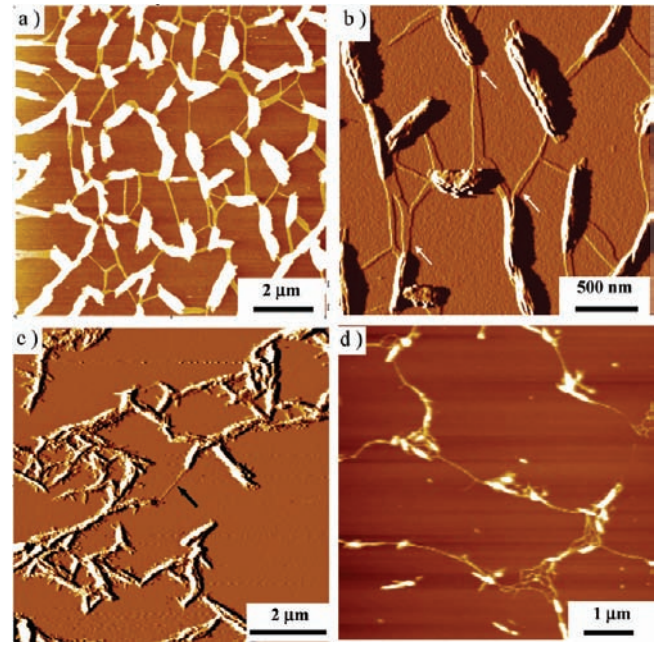

Figure 2. AFM height images of (a) blend of M-PDI:P-PDI (17% w/w) deposited from THF on Si/SiO_x. (b) Magnification of (a) showing M-PDI crystals connected by P-PDI chains. White arrows show the P-PDI chain originating from the short end of a M-PDI crystal. Image is gradient filtered to better show large and small features. (c) M-PDI:P-PDI (17% w/w) deposited from THF on mica. Black arrow shows a P-PDI chain not covered by M-PDI crystals. Image is gradient filtered to better show large and small features. (d) M-PDI:P-PDI (17% w/w) prepared by a two-step deposition, consisting of an initial deposition of P-PDI from a solution in THF on Si/SiO_x followed by deposition of a saturated solution of M-PDI in MeOH. *Z*-scales: (a) 12 nm, (b) 0.85 nm/nm, (c) 0.4 nm/nm, (d) 28 nm.

bundles, on which the monomers are forced to crystallize in small, disordered assemblies (Scheme 2c).

A bicomponent blend of M-PDI (500 mg/L) and P-PDI (75 mg/L, 15% w/w) was deposited on mica from a $CHCl_3$ solution; the AFM image of the resulting structures is shown in Figure 1a. It reveals a pattern of M-PDI crystalline islands bridged by P-PDI chains randomly positioned on the substrate. The polymers appear to be in close contact with the crystals, in some cases passing over and in some cases beneath them. We note that the morphologies of M-PDI and P-PDI do not seem to be disturbed by each other. The bicomponent sample appears as a superimposition of the individual arrangements of each component (Scheme 2a), with the M-PDI forming crystals similar to those which have been found in monocomponent M-PDI samples (Figure S1b), whereas the polymers are randomly distributed and oriented on the overall surface.

Changing the deposition solvent for M-PDI and P-PDI strongly affected the self-assembly behavior on the surface, underscoring an altered interaction between the two molecular systems. When M-PDI was codeposited from THF together with P-PDI (15% w/w), a network of the two components was observed in the final film on Si/SiO_x. In contrast to the $CHCl_3$/mica results, the P-PDI fibers did not appear to be randomly oriented on the Si/SiO_x surface (Figure 2a,b). The M-PDI crystals tended to induce the orientation of the P-PDI chains, forcing them to stretch from a M-PDI crystal to either another crystal or to a polymer chain. In the majority of the cases the P-PDI chain originated from the short end of a M-PDI crystal (see arrows in Figure 2b). This unique morphology can be seen as an array of M-PDI crystals connected by P-PDI chains. The overall arrangement and dimensions of the structures were similar to those of the monocomponent M-PDI sample deposited from THF (Figure S1c) and it can be assumed, therefore, that the structures are dictated by the self-assembly behavior of the monomer (Scheme 2b).

A distinct change of morphology was observed upon using THF as a solvent and mica as a substrate. The polymer appeared to adsorb first on the surface, with the M-PDI crystallizing preferentially on the adsorbed chains, forming a percolated network of small crystals, aligned to the underlying P-PDI (Figure 2c). The arrangement of the M-PDI crystals was similar to the random networks formed by the single component P-PDI samples on Si/SiO_x or mica (Figure S2). Consequently, it can be assumed that the morphology is dictated by the assembly behavior of P-PDI on the substrate surface, which subsequently templates the crystallization of the M-PDI (Scheme 2c).

This last result can be compared with an additional test experiment, in which the polarity of the system is further increased, i.e. by a two-step process using a combination of MeOH and THF on Si/SiO_x for the deposition of M-PDI and P-PDI. By subsequential deposition of P-PDI and M-PDI (i.e., having first the deposition of the polymer followed by the deposition of the monomer), M-PDI crystals are mainly observed on the pathways formed by the underlying P-PDI network (Figure 2d).

From the above experiments it can be concluded that subtle changes in the M-PDI and P-PDI interactions, as tuned by the employed solvent−substrate combination, can lead to all three different deposition scenarios mentioned above, i.e. (i) neither M-PDI nor P-PDI influence each other's morphology (in the case of $CHCl_3$ as solvent and mica as substrate, Scheme 2a), (ii) M-PDI governs the morphology, thereby forcing P-PDI chains to stretch between different nanocrystals (in the case of the combination THF and Si/SiO_x, Scheme 2b), and finally (iii) P-PDI determines the morphology, obliging M-PDI to form smaller crystals nucleated over P-PDI fiber network (as observed in the case of THF and mica, Scheme 2c). By applying these different experimental conditions, one can force M-PDI to

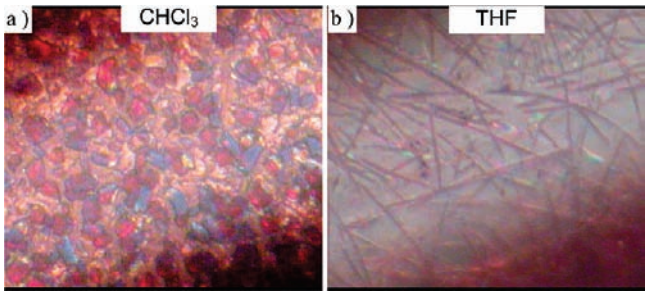

Figure 3. Optical microscopy images of bulk monomeric M-PDI samples in glass capillaries, recrystallized from (a) $CHCl_3$, (b) THF. Images sizes 136 μm × 121 μm.

determine the position and orientation of P-PDI and *vice versa*, thus organizing the same material in markedly different architectures at the macroscopic level.

3.2. X-ray Diffraction and Optical Microscopy Characterization. Molecule−surface interactions play a fundamental role structurally ordering thin films on solid substrates. To unveil the effect of reduced dimensionality and of the surface interactions, the self-assembly of M-PDI in thin layers on surfaces was compared with the self-assembly of this compound in bulk samples, where no macroscopic interface is present and the nanocrystals feature a random orientation in space. Optical microscopy (OM) images exhibited remarkably different morphologies: by using $CHCl_3$ as solvent isotropic macroscopic agglomerates were produced, whereas by employing THF and MeOH more anisotropic needles were formed (Figure 3 and Figure S3). Despite several attempts, no single crystal with a size sufficient to carry out a complete structure determination was obtained. Experiments performed on a single crystal diffractometer by using fibers consisting of a few almost isooriented crystals did allow us to determine the unit cell of the M-PDI structure. M-PDI crystallizes in the triclinic system, with lattice parameters $a = 17.58 \pm 0.09$ Å, $b = 10.73 \pm 0.06$ Å, $c = 7.58 \pm 0.05$ Å, $\alpha = 90.04 \pm 0.08°$, $\beta = 77.48 \pm 0.10°$, $\gamma = 79.63 \pm 0.11°$ and $V = 1375 \pm 20$ Å^3. The cell volume is comparable to that reported for *N*,*N*′-bis(2-methylbuthyl)-perylene-3,4:9,10-bis(dicarboximide),[50] and it is consistent with the presence of two PDI molecules per unit cell. No XRD characterization was performed on amorphous P-PDI, whose internal structure and chromophore packing had already been studied using more suitable spectroscopic techniques.[31,32]

Overall, while the morphology on the macroscopic scale is markedly different, common crystal features for all the samples grown from the different solvents were found by XRD, showing the same typical diffraction pattern (Figure S4a). Thus, although the morphology on meso- and macroscopic scale is significantly influenced by the solvent used for crystal growth, no differences in packing were found on the molecular scale. This indicates that the M-PDI crystals deposited from different solvents, albeit varying in dimension and shape, all possess the same molecular structure, and thus any differences in charge transport can be ascribed to differences in morphology on the micrometer scale and to the presence of the P-PDI polymer chains.

3.3. KPFM Studies on Bicomponent Systems. In contrast to blends for photovoltaics, which need a rather large difference in energetic levels between the two components to yield charge separation,[22,51−54] the M-PDI:P-PDI blend will need only a small energy difference in order to minimize the presence of the potential barrier to the flow of electrons at the interfaces between the different nanostructures. In principle, although the valence and the conductive energy levels of monomeric and polymeric aggregates depend on the PDI molecules stacking (i.e., electronic coupling),[55] their energetics are rather similar.[30] To assess this issue with a spatial resolution on the tens of nanometers scale, we measured the difference in work functions (WF) in our bicomponent layer materials by KPFM, where the WF of these semiconducting systems is defined as the difference between the intrinsic Fermi level and the vacuum level.

In the case of an organic self-assembled nanostructure, the surface potential (SP) of the object is defined as the sum of the work function difference between the tip and sample and the tip-induced polarization.[46] Both terms depend on the molecular packing of the PDIs in the aggregate. The topographic and the corresponding KPFM of bicomponent M-PDI and P-PDI films, which were previously reported as neat films in refs 56 and 57, respectively, are shown in Figure 1b,c. The KPFM displays a difference in the surface potential (SP) of the two materials, which can be ascribed to a different molecular packing, and thus to different HOMO−LUMO levels of the PDI moieties in the two phases of the blend.[55]

The contribution of the P-PDI has been separated from its surroundings with the help of a 2D deconvolution procedure as previously described[58] (see Supporting Information) and the obtained ΔSPs were found to range from 70 ± 15 mV. This value does not depend on the substrate on which the PDIs blend is deposited (mica or Si/SiO_x). The error bar is the variance obtained by averaging over all the collected measurements on the different substrates and different solvents used.

This is well within the range in which an Ohmic contact can be formed (0.3 eV or less), and hence the charge transport is expected to be facilitated.

3.4. Charge Transport in Thin Film Transistors. The electron charge mobility of nanocrystalline layers of M-PDI was measured by depositing this material as the electroactive layer in a TFT configuration. A slightly higher concentration of M-PDI nanocrystals was used with respect to the previously reported morphology studies, in order to have a higher concentration of M-PDI nanocrystals, and thus good percolation paths. Different TFTs devices were prepared using M-PDI either with or without P-PDI linkers and after surface morphology characterization by AFM the charge mobilities were investigated. These devices were not intended to reach *state of the art*

(50) Hadicke, E.; Graser, F. *Acta Crystallogr., Sect. C: Cryst. Struct. Commun.* **1986**, *42*, 189–195.
(51) Halls, J. J. M.; Walsh, C. A.; Greenham, N. C.; Marseglia, E. A.; Friend, R. H.; Moratti, S. C.; Holmes, A. B. *Nature* **1995**, *376*, 498–500.
(52) Palermo, V.; Ridolfi, G.; Talarico, A. M.; Favaretto, L.; Barbarella, G.; Camaioni, N.; Samorì, P. *Adv. Funct. Mater.* **2007**, *17*, 472–478.
(53) Chiesa, M.; Bürgi, L.; Kim, J. S.; Shikler, R.; Friend, R. H.; Sirringhaus, H. *Nano Lett.* **2005**, *5*, 559–563.
(54) Hoppe, H.; Glatzel, T.; Niggemann, M.; Hinsch, A.; Lux-Steiner, M. C.; Sariciftci, N. S. *Nano Lett.* **2005**, *5*, 269–274.
(55) Brédas, J. L.; Beljonne, D.; Coropceanu, V.; Cornil, J. *Chem. Rev.* **2004**, *104*, 4971–5003.
(56) Liscio, A.; De Luca, G.; Nolde, F.; Palermo, V.; Müllen, K.; Samorì, P. *J. Am. Chem. Soc.* **2008**, *130*, 780–781.
(57) Palermo, V.; Otten, M. B. J.; Liscio, A.; Schwartz, E.; de Witte, P. A. J.; Castriciano, M. A.; Wienk, M. M.; Nolde, F.; De Luca, G.; Cornelissen, J. J. L. M.; Janssen, R. A. J.; Müllen, K.; Rowan, A. E.; Nolte, R. J. M.; Samorì, P. *J. Am. Chem. Soc.* **2008**, *130*, 14605–14614.
(58) Liscio, A.; Palermo, V.; Samorì, P. *Adv. Funct. Mater.* **2008**, *18*, 907–914.

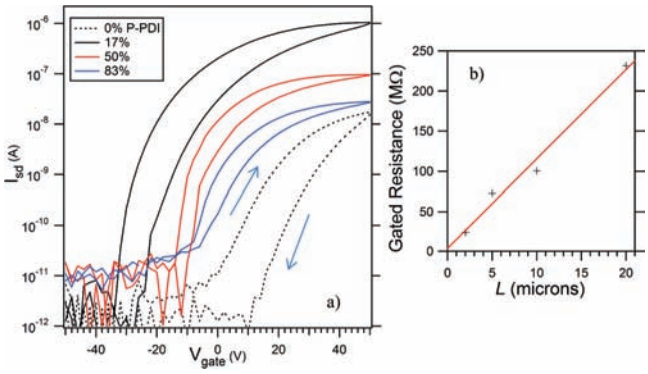

Figure 4. (a) Transfer characteristics, at source-drain bias of 25 V, of P-PDI:M-PDI TFTs with varying weight fractions of P-PDI, as indicated. The channel length was 2 μm in each case, and the direction of gate-voltage sweep is indicated by the arrows. (b) Gated resistance, defined as V_{sd}/I_{sd} at $V_{gate} = +50$ V, as a function of channel length (L), for the case of 17% P-PDI. The inferred contact resistance at $L = 0$ is 4.6 MΩ.

charge mobilities (due to the tiny amounts of material that were deposited and the incomplete coverage of the surface) but rather to compare the charge transport behavior of different blend architectures, i.e. with and without polymeric P-PDI linkers (Figure S5).

Figure 4 shows the TFT transfer plots for various M-PDI:P-PDI blend devices having respective ratios of 1:0, 5:1, 1:1, and 1:5 (in percent, 0%, 17%, 50%, and 83% P-PDI weight−weight concentration). Performance of a 100% P-PDI network is shown instead in Figure S6.

By adding 17% of P-PDI linker to the blend, the n-type transconductance of devices was observed to increase by around 2 orders of magnitude relative to monocomponent M-PDI film ("0%") devices, with the results showing a good level of reproducibility. While some caution must be exercised in applying the standard calculations for thin-films to the present situation, where there is incomplete coverage of the transistor channel, the notional linear-regime mobility (μ) increased by about 2 orders of magnitude (from $\mu \approx 5 \times 10^{-6}$ cm^2/(V s), to $\mu \approx 1 \times 10^{-4}$ cm^2/(V s) for 17% P-PDI). Although these charge mobilities are not high in absolute terms, the increase between the M-PDI and the M-PDI:P-PDI based devices is highly significant. The best M-PDI:P-PDI (17% P-PDI) devices showed an on/off ratio of order 10^4 to 10^5 and a subthreshold swing of ~4.5 V/decade; these compare with values of ~10^3 and ~12 V/dec respectively for devices incorporating neat M-PDI.

Additionally, we find that the "50%" P-PDI devices also give some improvement over M-PDI monocomponent film, although not as great as for the 17% case. For devices where the P-PDI fraction is 83%, the behavior begins to resemble the sparse "100%" P-PDI devices (Figure S6), which have very high gating thresholds and extreme hysteresis and show evidence of "bias-stress",[4] as large gating fields are applied to a network of the material which is thinner than the usual accumulation layer in the corresponding TFT device. Physically, carriers are trapped at interchain "bottlenecks" faster than they are gated into the film at high V_{gate}, effectively causing the threshold to shift to more positive values as V_{gate} increases.[4,59] If currents are limited by interchain processes, we still have a high number of "junctions" (trapping sites) in a sparse P-PDI 2 or 5 μm channel device. In this circumstance, the calculated mobility of devices is typically very low (10^{-7} cm^2/(V s), or worse). Therefore, in addition to the improved connectivity between the M-PDI aggregates, the P-PDI:M-PDI blend architecture also reduces the free-path of charge transport in the P-PDI phase to less than the average chain length, hence removing the adverse influence of bias-stress.

The output characteristics (Figure S7) of the devices show some nonlinearity in source-drain conductance at small source-drain bias, indicating that the measured gated channel-resistances and mobilities may be significantly limited by charge injection barriers at the channel−electrode interfaces. In order to better understand the effects of contact resistance, the gated resistance of devices may be inferred from the measured transfer data, as a function of channel length (Figure S7a). In the case of the "17%" M-PDI:P-PDI devices, a clear Ohmic behavior can be seen (Figure 4b), with an extrapolated contact resistance of 4.6 ± 1.2 MΩ; this value is broadly consistent with recent studies of P-PDI transistors, with similar device architecture.[35] By contrast, the trend for M-PDI devices was found to be non-Ohmic, with gated resistances increasing superlinearly with channel length (L). As a further illustration of this, in Figure S7b it can be seen that the transconductance decreases by more than 1 order of magnitude between the cases of $L = 2$ μm and $L = 5$ μm and the transistor action ceases completely for devices with $L = 20$ μm. This behavior is consistent with a situation where the poor interconnectivity of the M-PDI structures results in the average percolation length of carriers being less than the overall device channel lengths. It may therefore be inferred that the observed increase in mobility in the M-PDI:P-PDI devices relative to M-PDI is not due to extrinsic factors, such as an improvement of contact resistance, but is rather due to the improved connectivity within the active layer of the device. It is also apparent that charge transport is not adversely limited by charge-trapping processes or injection barriers[60] at the bridging points between P-PDI and M-PDI phases, which is corroborated by the KPFM studies described above.

In the case of the 17% P-PDI blend, the devices are still operational even with longer channel lengths of $L = 20$ μm (Figure S7a). Indeed, these longer channel devices showed a more classical output behavior, as compared to the $I-V$ curvature due to "short-channel" effects, which we observed in the $L = 2$ μm case. The impressively large areas (i.e., 20 × 10,000 μm) over which we can achieve good uniformity and coverage of the M-PDI:P-PDI blend within device channels, giving good electrical connectivity and charge transport, suggests that such structures may be attractive for large area optoelectronics applications, i.e. photovoltaics. For example, the increase of connectivity and percolation path described above can be useful to improve charge transport in three-dimensional, PDI-based bulk heterojunction blends, in which the electron-accepting M-PDI nanocrystals are dispersed into a compatible electron donor matrix (polythiophene or similar), and device efficiency depends strongly on the ability of M-PDI crystal network to transport the generated electrons.[25]

Finally, we note that the hysteresis observed between the up-sweep and down-sweep plots of the output and transfer curves is similar to that observed in many n-type bottom-gate TFT devices,[48] and may be attributed to charge trapping at the interface between the semiconducting layer and the oxide

(59) Sung, A.; Ling, M. M.; Tang, M. L.; Bao, Z. A.; Locklin, J. *Chem. Mater.* **2007**, *19*, 2342–2351.

(60) Paloheimo, J.; Stubb, H.; Grönberg, L. *Synth. Met.* **1993**, *55−57*, 4198.

substrate. The limitations in device performance also mean that, generally, the saturation regime of device output cannot be attained within the accessible range of operating voltages. More sophisticated top-gate transistor designs may, in future studies, offer less hysteretic device performances.

A microscopic model of charge transport in this system (e.g., kinetic "Monte Carlo" simulation) would represent a task of great computational complexity, and we consider this to be beyond the scope of this report. However, a macroscopic approach, such as those adopted for model polycrystalline systems by Street et al.[61] and Russell et al.,[37] offers a more viable alternative.

As a first-order model of our blend system, we consider the M-PDI nanocrystals as being evenly distributed in the transistor channel, with the spacing between them determined by the surface coverage (as may be inferred from AFM characterization), and the gaps between crystals being spanned by the network of P-PDI bundles. Assuming the transport to be quasi one-dimensional in nature, we can use percolation theory to calculate the carrier mobility (μ_{path}) of the conductive pathways through the device, thus:

$$\mu_{path} = \frac{\mu_H \mu_L}{\mu_H f + \mu_L (1 - f)} \quad (1)$$

where μ_H and μ_L are the high mobility (M-PDI crystals) and relatively low mobility (P-PDI) components, and f is the fraction of the pathway contained within the low mobility phase. Outline results from this model are shown in Figure 5.

This model has limitations, as it does not account for the mutual connectivity of the M-PDI domains, due to their size and shape variation; nor is it is trivial to relate the weight fractions of the deposited components to the parameter f, due to the incomplete coverage of the substrate. However, taking into account the pertinent regime of surface coverage ($S \approx 50\%$) and suitable literature-based estimates of μ_H and μ_L,[19,35] we find the predicted mobility for the "17%" P-PDI:M-PDI devices to be $\sim 10^{-4}$ cm^2/(V s), in good agreement with experiment.

Finally, it must be underlined that the P-PDI is a poor charge transporter if used alone in ultrathin layers ($\mu \approx 10^{-7}$ cm^2/(V s)), and it could in theory act as a bottleneck for charge transport in M-PDI.

Instead, by adding just a 17% of this polymer to M-PDI, an increase of charge mobility of 2 orders of magnitude (from 10^{-6} cm^2/(V s) to 10^{-4} cm^2/(V s)) is obtained, representing a clear demonstration that the performance of a material can be improved even by blending it with a lesser performing, but more percolating, additive.

Conclusions

The self-assembly of M-PDI on surfaces has been studied by using various solvents and employing different substrates. The surface morphology of M-PDI was found to be correlated to the polarity of the solvent and the substrate, with the formation of a continuous, amorphous layer when the combination $CHCl_3/SiO_x$ (less polar, larger affinity) was used, and the formation of thicker, less dense crystals when the combination MeOH/mica (more polar, smaller affinity) was applied. The interplay between M-PDI and its polymeric derivative P-PDI during the deposition could be successfully controlled by tuning the solvent and substrate polarity. While

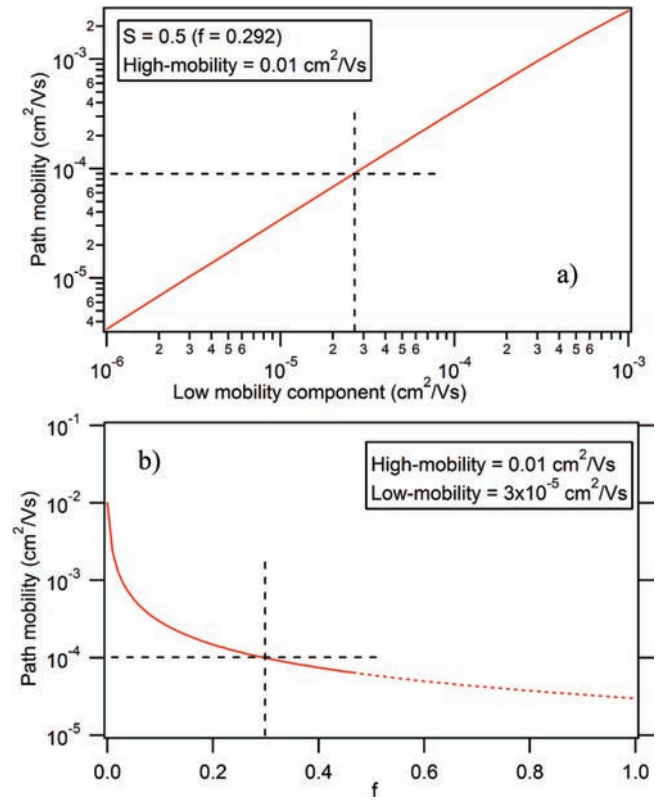

Figure 5. Results of a simple 1D transport model of M-PDI:P-PDI blends, showing (a) the expected dependence of path mobility on the low mobility (P-PDI) component, based on a M-PDI surface coverage (S) of 50% and (b) the expected dependence of path mobility on the filling fraction of the P-PDI component. The dotted section of the plot indicates where the spacing between PDI crystals has become greater than the average P-PDI strand length (~180 nm), and we expect interchain trapping to become prohibitive; this corresponds to $S \leq 0.277$, $f \geq 0.474$. For both graphs, the measured device mobility value of $\sim 10^{-4}$ cm^2/(V s) is marked with a dashed guideline.

for the combination $CHCl_3$/mica the two components do not influence each others' morphology, this is not the case when the polarity of the solvent and/or the substrate is increased. By using the solvent−substrate combination THF/SiO_x, the P-PDI could be forced to act as a linker that bridges different neighboring M-PDI nanocrystals, whereas with the even more polar combination THF/mica it was possible to force PDI crystallization over the polymer, to form random well-percolated networks. KPFM analysis showed minimal differences in surface potential between the two phases, which suggests a low potential barrier for charge transport. As a result of this, TFT studies revealed a remarkable improvement in device connectivity and a 2 orders of magnitude enhancement of the n-type charge mobility of the M-PDI:P-PDI blend, as compared to that of M-PDI itself. Hence, such a controlled formation of percolation pathways for charge transport offers an attractive strategy to improve the performance of electronic devices. Of a more fundamental interest, our technique allows the bridging of semiconducting crystals, without the formation of prohibitive charge-trapping sites or injection barriers at the connection points. The strategy presented here for promoting charge transport in polycrystalline films for organic electronics is not limited to PDI electroactive derivatives, and can be more generally applied to any combination of a small electroactive molecule and its polymeric analog that is linked to a rigid scaffold, including

(61) Street, R. A.; Northrup, J. E.; Salleo, A. *Phys. Rev. B* **2005**, *71*, 165202.

high performance molecular moieties such as thiophenes or polyfluorenes.

Acknowledgment. This work was supported by the ESF-SONS2-SUPRAMATES and the EU through the projects Marie Curie IEF-HESPERUS (PIEF-GA-2008-219770), EST-SUPER (MEST-CT-2004-008128), the ERA-Chemistry project SurConFold, and the Regione Emilia-Romagna PRIITT Nanofaber Net-Lab, The Netherlands Organization for Scientific Research Chemistry Section (top grant to R.J.M.N and Vici Grant to A.E.R), Nanoned STW (grants to R.J.M and A.E.R.), and the Royal Netherlands Academy for Arts and Sciences (R.J.M.N.). C.E.F. thanks the Leverhulme Trust (UK) for an *Early Career Fellowship*.

Supporting Information Available: Self-assembly of mono-component M-PDI films on surfaces; quantitative potential measurements using KPFM; X-ray diffraction and optical microscopy characterization; table S1 and Figures S1−S7; complete ref 32.This material is available free of charge via the Internet at http://pubs.acs.org.

JA809731E